GEOMETRIC NETWORKS INDUCED BY ENERGY CONSTRAINED DIFFUSION

Anonymous authors
Paper under double-blind review

ABSTRACT

Real-world data generation often involves complex inter-dependencies among instances, violating the IID-data hypothesis of standard learning paradigms and posing a challenge for uncovering the geometric structures for learning desired instance representations. To this end, we introduce an energy constrained diffusion model which encodes *a batch of instances* from a dataset into evolutionary states that progressively incorporate other instances' information by their interactions. The diffusion process is constrained by descent criteria w.r.t. a principled energy function that characterizes the global consistency of instance representations over latent structures. We provide rigorous theory that implies closed-form optimal estimates for the pairwise diffusion strength among arbitrary instance pairs, which gives rise to a new class of neural encoders, dubbed as DIFFORMER, with two instantiations: a simple version with linear complexity for prohibitive instance numbers, and an advanced version for learning complex structures. Experiments highlight the wide applicability of our model as a general-purpose encoder backbone with superior performance in various tasks, such as semi-supervised node classification, image/text classification, and spatial-temporal dynamics prediction.

1 INTRODUCTION

Real-world data are generated from a convoluted interactive process whose underlying physical principles are often unknown. Such a nature violates the common hypothesis of standard representation learning paradigms assuming that data are IID sampled. The challenge, however, is that due to the absence of prior knowledge about ground-truth data generation, it can be practically prohibitive to build feasible methodology for uncovering data dependencies, despite the acknowledged significance. To address this issue, prior works, e.g., Wang et al. (2019); Franceschi et al. (2019); Jiang et al. (2019b); Zhang et al. (2019), consider encoding the potential interactions between instance pairs, but this requires sufficient degrees of freedom that significantly increases learning difficulty from limited labels (Fatemi et al., 2021) and hinders the scalability to large systems (Chen et al., 2020c).

Turning to a simpler problem setting where putative instance relations are instantiated as an observed graph, remarkable progress has been made in designing expressive architectures such as graph neural networks (GNNs) (Scarselli et al., 2008; Kipf & Welling, 2017; Velickovic et al., 2018; Wu et al., 2019; Chen et al., 2020a; Yang et al., 2021) for harnessing inter-connections between instances as a geometric prior (Bronstein et al., 2017). However, the observed relations can be incomplete/noisy, due to error-prone data collection, or generated by an artificial construction independent from downstream targets. The potential inconsistency between observation and the underlying data geometry would presumably elicit systematic bias between structured representation of graph-based learning and true data dependencies. While a plausible remedy is to learn more useful structures from the data, this unfortunately brings the previously-mentioned obstacles to the fore.

To resolve the dilemma, we propose a novel general-purpose encoder framework that uncovers data dependencies from observations (a dataset of partially labeled instances), proceeding via two-fold inspiration from physics as illustrated in Fig. 1. Our model is defined through feed-forward continuous dynamics (i.e., a PDE) involving all the instances of a dataset as locations on Riemannian manifolds with *latent* structures, upon which the features of instances act as heat flowing over the underlying geometry (Hamzi & Owhadi, 2021). Such a diffusion model serves an important *inductive bias* for leveraging global information from other instances to obtain more informative representations.

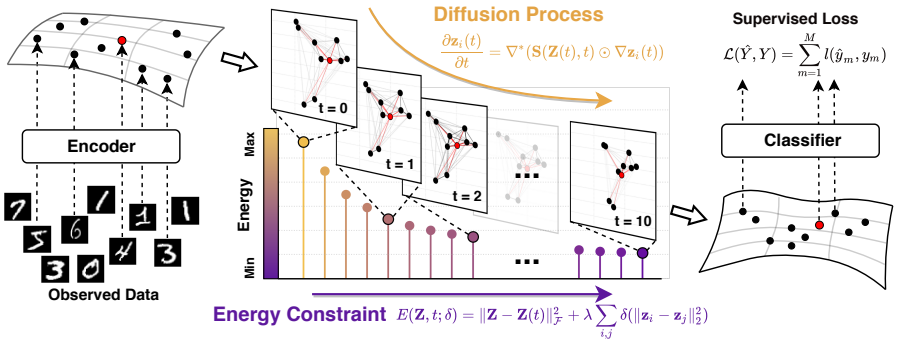

Figure 1: An illustration of the general idea behind DIFFORMER which takes a whole dataset (or a batch) of instances as input and encodes them into hidden states through a diffusion process aimed at minimizing a regularized energy. This design allows feature propagation among arbitrary instance pairs at each layer with optimal inter-connecting structures for informed prediction on each instance.

Its major advantage lies in the flexibility for the *diffusivity* function, i.e., a measure of the rate at which information spreads (Rosenberg & Steven, 1997): we allow for feature propagation between arbitrary instance pairs at each layer, and adaptively navigate this process by pairwise connectivity weights. Moreover, for guiding the instance representations towards some ideal constraints of internal consistency, we introduce a principled energy function that enforces layer-wise *regularization* on the evolutionary directions. The energy function provides another view (from a macroscopic standpoint) into the desired instance representations with low energy that are produced, i.e., soliciting a steady state that gives rise to informed predictions on unlabeled data.

As a justification for the tractability of above general methodology, our theory reveals the underlying equivalence between finite-difference iterations of the diffusion process and unfolding the minimization dynamics for an associated regularized energy. This result further suggests a closed-form optimal solution for the diffusivity function that updates instance representations by the ones of all the other instances towards giving a rigorous decrease of the global energy. Based on this, we also show that the energy constrained diffusion model can serve as a principled perspective for unifying popular models like MLP, GCN and GAT which can be viewed as special cases of our framework.

On top of the theory, we propose a new class of neural encoders, Diffusion-based Transformers (DIFFORMER), and its two practical instantiations: one is a simple version with $\mathcal{O}(N)$ complexity (N for instance number) for computing all-pair interactions among instances; the other is a more expressive version that can learn complex latent structures. We empirically demonstrate the success of DIFFORMER on a diverse set of tasks. It outperforms SOTA approaches on semi-supervised node classification benchmarks and performs competitively on large-scale graphs. It also shows promising power for image/text classification with low label rates and predicting spatial-temporal dynamics.

2 RELATED WORK

Graph-based Semi-supervised Learning. Graph-based SSL (Kipf & Welling, 2017) aims to learn from partially labeled data, where instances are treated as nodes and their relations are given by a graph. The observed structure can be leveraged as regularization for learning representations (Belkin et al., 2006; Weston et al., 2012; Yang et al., 2016) or as an inductive bias of modern GNN architectures (Scarselli et al., 2008). However, there frequently exist situations where the observed structure is unavailable or unreliable (Franceschi et al., 2019; Jiang et al., 2019b; Zhang et al., 2019; Chen et al., 2020c; Fatemi et al., 2021), in which case the challenge remains how to uncover the underlying relations. This paper explores a new encoder architecture for discovering data geometry to promote learning through the inter-dependence among instances (either labeled or unlabeled).

Neural Diffusion Models. There are several recent efforts on diffusion-based learning where continuous dynamics serve as an inductive bias for representation learning (Hamzi & Owhadi, 2021). One category directly solves a continuous process of differential equations (Lagaris et al., 1998; Chen et al., 2018), e.g., Chamberlain et al. (2021a) and its follow-ups (Chamberlain et al., 2021b; Thorpe et al., 2022) reveal the analogy between the discretization of diffusion process and GNNs' feedforward rules, and devise new (continuous) models on graphs whose training requires PDE-solving tools. Differently, another category is PDE-inspired learning using the diffusion perspective

as motivation on top of which new (discrete) graph neural models are designed (Atwood & Towsley, 2016; Tsitsulin et al., 2018; Klicpera et al., 2019; Xu et al., 2020; Wang et al., 2021). Our work leans on the latter and the key originality lies in two aspects. First, we introduce a novel diffusion model whose dynamics are implicitly defined by optimizing a regularized energy. Second, our theory establishes an equivalence between the numerical iterations of diffusion process and unfolding the optimization of the energy, based on which we develop a new class of neural encoders for uncovering latent structures among a layer number of instances.

Instance/Node-Level v.s. Graph-Level Prediction. To avoid potential mis-interpretations of our work, we remark upfront that our goal is to learn a single latent interaction graph among instances, and this can be generally viewed as an embodiment of *node-level* prediction (NP) tasks widely studied in the graph learning community. This is distinct from *graph-level* prediction (GP) whereby each graph itself generally has a single label to predict and a dataset contains many graph instances. These two problems are typically tackled separately in the literature (Hu et al., 2020) with disparate technical considerations. This is because input instances are inter-dependent in NP (due to the instance interactions involved in the data-generating process), while in GP tasks the instances can be treated as IID samples. Although there exist some recent models considering all-pair feature propagation among the nodes of each graph instance (Wang et al., 2019; Dwivedi & Bresson, 2020), such prior work largely focuses on GP with relatively small graphs. It therefore remains under-explored how to build an efficient and expressive model for learning node-pair interactions for NP tasks involving latent graphs that can be prohibitively large.

3 Energy Constrained Geometric Diffusion Transformers

Consider a set of partially labeled instances $\{\mathbf{x}_i\}_{i=1}^N$, whose labeled portion is $\{(\mathbf{x}_j, y_j)\}_{j=1}^M$ (often $M \ll N$). In some cases there exists relational structures that connect instances as a graph $\mathcal{G} = (\mathcal{V}, \mathcal{E})$, where the node set $\mathcal{V}$ contains all the instances and the edge set $\mathcal{E} = \{e_{ij}\}$ consists of observed relations. Without loss of generality, the main body of this section does *not* assume graph structures as input, but we will later discuss how to trivially incorporate then if/when available.

3.1 Geometric Diffusion Model

The starting point of our model is a diffusion process that treats a dataset of instances as a whole and produces instance representations through information flows characterized by an anisotropic diffusion process, which is inspired by an analogy with heat diffusion on a Riemannian manifold (Rosenberg & Steven, 1997). We use a vector-valued function $\mathbf{z}_i(t) : [0, \infty) \to \mathbb{R}^d$ to define an instance's state at time t and location i. The anisotropic diffusion process describes the evolution of instance states (i.e., representations) via a PDE with boundary conditions (Freidlin & Wentzell, 1993; Medvedev, 2014):

$$\frac{\partial \mathbf{Z}(t)}{\partial t} = \nabla^* \left(\mathbf{S}(\mathbf{Z}(t), t) \odot \nabla \mathbf{Z}(t) \right), \quad \text{s. t. } \mathbf{Z}(0) = [\mathbf{x}_i]_{i=1}^N, \quad t \geq 0, \tag{1}$$

where $\mathbf{Z}(t) = [\mathbf{z}_i(t)]_{i=1}^N \in \mathbb{R}^{N \times d}$, $\odot$ denotes the Hadamard product, and the function $\mathbf{S}(\mathbf{Z}(t), t) : \mathbb{R}^{N \times d} \times [0, \infty) \to [0, 1]^{N \times N}$ defines the *diffusivity* coefficient controlling the diffusion strength between any pair at time t. The diffusivity is specified to be dependent on instances' states. The gradient operator ∇ measures the difference between source and target states, i.e., $(\nabla \mathbf{Z}(t))_{ij} = \mathbf{z}_j(t) - \mathbf{z}_i(t)$, and the divergence operator ∇^* sums up information flows at a point, i.e., $(\nabla^*)_i = \sum_{j=1}^N \mathbf{S}_{ij}(\mathbf{Z}(t), t) \left(\nabla \mathbf{Z}(t)\right)_{ij}$. Note that both operators are defined over a discrete space consisting of N locations. The physical implication of Eq. 1 is that the temporal change of heat at location i equals to the heat flux that spatially enters into the point. Eq. 1 can be explicitly written as

$$\frac{\partial \mathbf{z}_i(t)}{\partial t} = \sum_{j=1}^N \mathbf{S}_{ij}(\mathbf{Z}(t), t)(\mathbf{z}_j(t) - \mathbf{z}_i(t)). \tag{2}$$

Such a diffusion process can serve as an inductive bias that guides the model to use other instances' information at every layer for learning informative instance representations. We can use numerical methods to solve the continuous dynamics in Eq. 2, e.g., the explicit Euler scheme involving finite differences with step size τ, which after some re-arranging gives:

$$\mathbf{z}_i^{(k+1)} = \left(1 - \tau \sum_{j=1}^N \mathbf{S}_{ij}^{(k)} \right) \mathbf{z}_i^{(k)} + \tau \sum_{j=1}^N \mathbf{S}_{ij}^{(k)} \mathbf{z}_j^{(k)}. \tag{3}$$

The numerical iteration can stably converge for $\tau \in (0, 1)$. We can adopt the state after a finite number K of propagation steps and use it for final predictions, i.e., $\hat{y}_i = \text{MLP}(\mathbf{z}_i^{(K)})$.

Remark. The diffusivity coefficient in Eq. 1 is a measure of the rate at which heat can spread over the space (Rosenberg & Steven, 1997). Particularly in Eq. 2, $\mathbf{S}(\mathbf{Z}(t), t)$ determines how information flows over instances and the evolutionary direction of instance states. Much flexibility remains for its specification. For example, a basic choice is to fix $\mathbf{S}(\mathbf{Z}(t), t)$ as an identity matrix which constrains the feature propagation to self-loops and the model degrades to an MLP that treats all the instances independently. One could also specify $\mathbf{S}(\mathbf{Z}(t), t)$ as the observed graph structure if available in some scenarios. In such a case, however, the information flows are restricted by neighboring nodes in a graph. An ideal case could be to allow $\mathbf{S}(\mathbf{Z}(t), t)$ to have non-zero values for arbitrary (i, j) and evolve with time, i.e., the instance states at each layer can efficiently and adaptively propagate to all the others.

3.2 Diffusion Constrained by a Layer-wise Energy

As mentioned previously, the crux is how to define a proper diffusivity function to induce a desired diffusion process that can maximize the information utility and accord with some inherent consistency. Since we have no prior knowledge for the explicit form or the inner structure of $\mathbf{S}^{(k)}$, we consider the diffusivity as a time-dependent latent variable and introduce an *energy function* that measures the presumed quality of instance states at a given step k:

$$E(\mathbf{Z}, k; \delta) = \|\mathbf{Z} - \mathbf{Z}^{(k)}\|_{\mathcal{F}}^2 + \lambda \sum_{i,j} \delta(\|\mathbf{z}_i - \mathbf{z}_j\|_2^2), \tag{4}$$

where $\delta : \mathbb{R} \to \mathbb{R}$ is defined as a *non-decreasing* and *concave* function that promotes robustness against large differences (Yang et al., 2021) among any pair of instances. Eq. 4 assigns each state in $\mathbb{R}^d$ with an energy scalar which can be leveraged to regularize the updated states (towards lower energy desired). The weight λ trades two effects: 1) for each instance i, the states not far from the current one $\mathbf{z}_i^{(k)}$ have low energy; 2) for all instances, the smaller differences their states have, the lower energy is produced.

Remark. Eq. 4 can essentially be seen as a robust version of the energy introduced by Zhou et al. (2004), inheriting the spirit of regularizing the global and local consistency of representations. "Robust" here particularly implies that the δ adds uncertainty to each pair of the instances and could *implicitly* filter the information of noisy links (potentially reflected by proximity in the latent space).

Energy Constrained Diffusion. The diffusion process describes the *microscopic* behavior of instance states through evolution, while the energy function provides a *macroscopic* view for quantifying the consistency. In general, we expect that the final states could yield a low energy, which suggests that the physical system arrives at a steady point wherein the yielded instance representations have absorbed enough global information under a certain guiding principle. Thereby, we unify two schools of thoughts into a new diffusive system where instance states would evolve towards producing lower energy, e.g., by finding a valid diffusivity function. Formally, we aim to find a series of $\mathbf{S}^{(k)}$'s whose dynamics and constraints are given by

$$\begin{aligned} &\mathbf{z}_i^{(k+1)} = \left(1 - \tau \sum_{j=1}^{N} \mathbf{S}_{ij}^{(k)}\right) \mathbf{z}_i^{(k)} + \tau \sum_{j=1}^{N} \mathbf{S}_{ij}^{(k)} \mathbf{z}_j^{(k)} \\ &\text{s. t. } \mathbf{z}_i^{(0)} = \mathbf{x}_i, \quad E(\mathbf{Z}^{(k+1)}, k; \delta) \leq E(\mathbf{Z}^{(k)}, k-1; \delta), \quad k \geq 1. \end{aligned} \tag{5}$$

The formulation induces a new class of geometric flows on latent manifolds whose dynamics are *implicitly* defined by optimizing a time-varying energy function (see Fig. 1 for an illustration).

3.3 Tractability of Solving Diffusion Process with Energy Minimization

Unfortunately, Eq. 5 is hard to solve since we need to infer the value for a series of coupled $\mathbf{S}^{(k)}$'s that need to satisfy K inequalities by the energy minimization constraint. The key result of this paper is the following theorem that reveals the underlying connection between the geometric diffusion model and iterative minimization of the energy, which further suggests an explicit closed-form solution for $\mathbf{S}^{(k)}$ based on the current states $\mathbf{Z}^{(k)}$ that yields a rigorous decrease of the energy.

Theorem 1. *For any regularized energy defined by Eq. 4 with a given λ, there exists $0 < \tau < 1$ such that the diffusion process of Eq. 3 with the diffusivity between pair (i, j) at the k-th step given by*

$$\hat{\mathbf{S}}_{ij}^{(k)} = \frac{\omega_{ij}^{(k)}}{\sum_{l=1}^{N} \omega_{il}^{(k)}}, \quad \omega_{ij}^{(k)} = \left.\frac{\partial \delta(z^2)}{\partial z^2}\right|_{z^2 = \|\mathbf{z}_i^{(k)} - \mathbf{z}_j^{(k)}\|_2^2}, \tag{6}$$

yields a descent step on the energy, i.e., $E(\mathbf{Z}^{(k+1)}, k; \delta) \leq E(\mathbf{Z}^{(k)}, k-1; \delta)$ for any $k \geq 1$.

Theorem 1 suggests the existence for the optimal diffusivity in the form of a function over the l_2 distance between states at the current step, i.e., $\|\mathbf{z}_i^{(k)} - \mathbf{z}_j^{(k)}\|_2$. The result enables us to unfold the implicit process and compute $\mathbf{S}^{(k)}$ in a feed-forward way from the initial states. We thus arrive at a new family of neural model architectures with layer-wise computation specified by:

$$\begin{aligned} &\text{Diffusivity Inference:} \quad \hat{\mathbf{S}}_{ij}^{(k)} = \frac{f(\|\mathbf{z}_i^{(k)} - \mathbf{z}_j^{(k)}\|_2^2)}{\sum_{l=1}^{N} f(\|\mathbf{z}_i^{(k)} - \mathbf{z}_l^{(k)}\|_2^2)}, \quad 1 \leq i, j \leq N, \\ &\text{State Updating:} \quad \mathbf{z}_i^{(k+1)} = \underbrace{\left(1 - \tau \sum_{j=1}^{N} \hat{\mathbf{S}}_{ij}^{(k)}\right) \mathbf{z}_i^{(k)}}_{\text{state conservation}} + \underbrace{\tau \sum_{j=1}^{N} \hat{\mathbf{S}}_{ij}^{(k)} \mathbf{z}_j^{(k)}}_{\text{state propagation}}, \quad 1 \leq i \leq N. \end{aligned} \tag{7}$$

Remark. The choice of function f in above formulation is not arbitrary, but needs to be a non-negative and decreasing function of z^2, so that the associated δ in Eq. 4 is guaranteed to be non-decreasing and concave w.r.t. z^2. Critically though, there remains much room for us to properly design the specific f, so as to provide adequate capacity and scalability. Also, in our model presented by Eq. 7 we only have one hyper-parameter τ in practice, noting that the weight λ in the regularized energy is implicitly determined through τ by Theorem 1, which reduces the cost of hyper-parameter searching.

4 Instantiations of DIFFormer

4.1 Model Implementation

We next go into model instantiations based on our theory. We introduce two specified f's as practical versions of our model whose detailed implementations are given in Appendix D with PyTorch-style pseudo code. First, because $\|\mathbf{z}_i - \mathbf{z}_j\|_2^2 = \|\mathbf{z}_i\|_2^2 + \|\mathbf{z}_j\|_2^2 - 2\mathbf{z}_i^\top \mathbf{z}_j$, we can convert $f(\|\mathbf{z}_i - \mathbf{z}_j\|_2^2)$ into the form $g(\mathbf{z}_i^\top \mathbf{z}_j)$ using a change of variables on the condition that $\|\mathbf{z}_i\|_2$ remains constant. And we add layer normalization to each layer to loosely enforce such a property in practice.

Simple Diffusivity Model. A straightforward design is to adopt the linear function $g(x) = 1 + x$:

$$\omega_{ij}^{(k)} = f(\|\tilde{\mathbf{z}}_i^{(k)} - \tilde{\mathbf{z}}_j^{(k)}\|_2^2; W_Q^{(k)}, W_K^{(k)}) = 1 + (\mathbf{W}_Q^{(k)} \mathbf{z}_i^{(k)})^\top (\mathbf{W}_K^{(k)} \mathbf{z}_j^{(k)}), \tag{8}$$

where $\mathbf{W}_Q^{(k)}$, $\mathbf{W}_K^{(k)}$ are learnable weight matrices of the k-th layer. Assuming $\tilde{\mathbf{z}}_i^{(k)} = \mathbf{W}_Q^{(k)} \mathbf{z}_i^{(k)}$, $\tilde{\mathbf{z}}_j^{(k)} = \mathbf{W}_K^{(k)} \mathbf{z}_j^{(k)}$ and $z = \|\tilde{\mathbf{z}}_i^{(k)} - \tilde{\mathbf{z}}_j^{(k)}\|_2$, Eq. 8 can be written as $f(z^2) = 2 - \frac{1}{2} z^2$, which yields a non-negative result and is decreasing w.r.t. z^2.

One scalability concern for the model Eq. 7 arises because of the need to compute pairwise diffusivity and propagation for each individual, inducing $\mathcal{O}(N^2)$ complexity. Remarkably, the simple diffusivity model allows a significant acceleration by noting that the state propagation can be re-arranged via

$$\sum_{j=1}^{N} \mathbf{S}_{ij}^{(k)} \mathbf{z}_j^{(k)} = \sum_{j=1}^{N} \frac{1 + (\tilde{\mathbf{z}}_i^{(k)})^\top \tilde{\mathbf{z}}_j^{(k)}}{\sum_{l=1}^{N} \left(1 + (\tilde{\mathbf{z}}_i^{(k)})^\top \tilde{\mathbf{z}}_l^{(k)}\right)} \mathbf{z}_j^{(k)} = \frac{\sum_{j=1}^{N} \mathbf{z}_j^{(k)} + \left(\sum_{j=1}^{N} (\tilde{\mathbf{z}}_j^{(k)})^\top \mathbf{z}_j^{(k)}\right) \cdot \tilde{\mathbf{z}}_i^{(k)}}{N + (\tilde{\mathbf{z}}_i^{(k)})^\top \sum_{l=1}^{N} \tilde{\mathbf{z}}_l^{(k)}}. \tag{9}$$

Note that the two summation terms above can be computed once and shared to every instance i, reducing the complexity in each iteration to $\mathcal{O}(N)$. We call this implementation as DIFFormer-s.

Advanced Diffusivity Model. The simple model facilitates efficiency/scalability, yet may sacrifice the capacity for complex latent geometry. We thus propose an advanced version with $g(x) = \frac{1}{1+\exp(-x)}$:

$$\omega_{ij}^{(k)} = f(\|\tilde{\mathbf{z}}_i^{(k)} - \tilde{\mathbf{z}}_j^{(k)}\|_2^2; W_Q^{(k)}, W_K^{(k)}) = \frac{1}{1 + \exp\left(-(\mathbf{W}_Q^{(k)} \mathbf{z}_i^{(k)})^\top (\mathbf{W}_K^{(k)} \mathbf{z}_j^{(k)})\right)}, \tag{10}$$

Table 1: A unified view for MLP, GCN and GAT from our energy-driven geometric diffusion framework regarding energy function forms, diffusivity specifications and algorithmic complexity.

Models	Energy Function $E(\mathbf{Z}, k; \delta)$	Diffusivity $\mathbf{S}^{(k)}$	Complexity
MLP	$\|\mathbf{Z} - \mathbf{Z}^{(k)}\|_2^2$	$\mathbf{S}_{ij}^{(k)} = \begin{cases} 1, & \text{if } i = j \\ 0, & otherwise \end{cases}$	$\mathcal{O}(NKd^2)$
GCN	$\sum_{(i,j)\in\mathcal{E}} \|\mathbf{z}_i - \mathbf{z}_j\|_2^2$	$\mathbf{S}_{ij}^{(k)} = \begin{cases} \frac{1}{\sqrt{d_i d_j}}, & \text{if } (i,j) \in \mathcal{E} \\ 0, & otherwise \end{cases}$	$\mathcal{O}(\|\mathcal{E}\|Kd^2)$
GAT	$\sum_{(i,j)\in\mathcal{E}} \delta(\|\mathbf{z}_i - \mathbf{z}_j\|_2^2)$	$\mathbf{S}_{ij}^{(k)} = \begin{cases} \frac{f(\|\mathbf{z}_i^{(k)} - \mathbf{z}_j^{(k)}\|_2^2)}{\sum_{l:(i,l)\in\mathcal{E}} f(\|\mathbf{z}_i^{(k)} - \mathbf{z}_l^{(k)}\|_2^2)}, & \text{if } (i,j) \in \mathcal{E} \\ 0, & otherwise \end{cases}$	$\mathcal{O}(\|\mathcal{E}\|Kd^2)$
DIFFORMER	$\|\mathbf{Z} - \mathbf{Z}^{(k)}\|_2^2 + \lambda \sum_{i,j} \delta(\|\mathbf{z}_i - \mathbf{z}_j\|_2^2)$	$\mathbf{S}_{ij}^{(k)} = \frac{f(\|\mathbf{z}_i^{(k)} - \mathbf{z}_j^{(k)}\|_2^2)}{\sum_{l=1}^{N} f(\|\mathbf{z}_i^{(k)} - \mathbf{z}_l^{(k)}\|_2^2)}, \quad 1 \le i,j \le N$	DIFFORMER-s : $\mathcal{O}(NKd^2)$ DIFFORMER-a : $\mathcal{O}(N^2Kd^2)$

which corresponds with $f(z^2) = \frac{1}{1+e^{z^2/2-1}}$ guaranteeing monotonic decrease and non-negativity. We dub this version as DIFFORMER-a. Appendix C further compares the two models (i.e., different f's and δ's) through synthetic results. Real-world empirical comparisons are in Section 5.

4.2 MODEL EXTENSIONS AND FURTHER DISCUSSION

Incorporating Layer-wise Transformations. Eq. 7 does not use feature transformations for each layer. To further improve the representation capacity, we can add such transformations after the updating, i.e., $\mathbf{z}_i^{(k+1)} \leftarrow h^{(k)}(\mathbf{z}_i^{(k+1)})$ where $h^{(k)}$ can be a fully-connected layer (see Appendix D for details). In this way, each iteration of the diffusion yields a descent of a particular energy $E(\mathbf{Z}, k; \delta, h^{(k)}) = \|\mathbf{Z} - h^{(k)}(\mathbf{Z}^{(k)})\|_2^2 + \sum_{i,j} \delta(\|\mathbf{z}_i - \mathbf{z}_j\|_2^2)$ dependent on k. The diffusion process becomes a composition of a series of steps, each of which optimizes a locally adaptive energy. Although it breaks the layer-wise consistency via a globally shared energy function, the trainable transformation $h^{(k)}$ can be optimized w.r.t. the supervised loss to map the instance representations into a proper latent space. Our experiments find that the layer-wise transformation is not necessary for small datasets, but contributes to positive effects for datasets with larger sizes. Furthermore, one can consider non-linear activations in the layer-wise transformation $h^{(k)}$ though we empirically found that using a linear model already performs well. We also note that Theorem 1 can be extended to hold even when incorporating such a non-linearity in each layer (see Appendix B for detailed discussions).

Incorporating Input Graphs. For the model presented so far, we do *not* assume an input graph for the model formulation. For situations with observed structures as available input, we have $\mathcal{G} = (\mathcal{V}, \mathcal{E})$ that can be leveraged as a geometric prior. We can thus modify the updating rule as:

$$\mathbf{z}_i^{(k+1)} = \left(1 - \frac{\tau}{2}\sum_{j=1}^{N}\left(\hat{\mathbf{S}}_{ij}^{(k)} + \tilde{\mathbf{A}}_{ij}\right)\right)\mathbf{z}_i^{(k)} + \frac{\tau}{2}\sum_{j=1}^{N}\left(\hat{\mathbf{S}}_{ij}^{(k)} + \tilde{\mathbf{A}}_{ij}\right)\mathbf{z}_j^{(k)}, \tag{11}$$

where $\tilde{\mathbf{A}}_{ij} = \frac{1}{\sqrt{d_i d_j}}$ if $(i,j) \in \mathcal{E}$ and 0 otherwise, and d_i is instance i's degree in $\mathcal{G}$. The diffusion iteration of Eq. 11 is equivalent to minimizing a new energy additionally incorporating a graph-based penalty (Ioannidis et al., 2017), i.e., $\sum_{(i,j)\in\mathcal{E}} \|\mathbf{z}_i^{(k)} - \mathbf{z}_j^{(k)}\|_2^2$ (see Appendix C for details).

Scaling to Large Datasets. Another advantage of DIFFORMER is the flexibility for mini-batch training. For datasets with prohibitive instance numbers that make it hard for full-batch training on a single GPU, we can naturally partition the dataset into mini-batches and feed one mini-batch for one feed-forward and backward computation. Similar efforts can be applied for parallel acceleration.

Connection with Existing Models. The proposed methodology in fact serves as a general diffusion framework that provides a unifying view whereby some existing models can be seen as special cases of ours. As a non-exhaustive summary and high-level comparison, Table 1 presents the relationships with MLP, GCN and GAT which can be expressed via simplified versions of our principled energy and diffusion models (see more elaboration in Appendix E).

Table 2: Mean and standard deviation of testing accuracy on node classification (with five different random initializations). All the models are split into groups with a comparison of non-linearity (whether to use activation for layer-wise transformations), continuity (whether the model is continuous and requires PDE-solver for back-propagation) and rewiring (whether to modify the structure).

Type	Model	Non-linearity	Continuity	Rewiring	Cora	Citeseer	Pubmed
Basic models	MLP	✔	-	-	56.1 ± 1.6	56.7 ± 1.7	69.8 ± 1.5
	LP	-	-	-	68.2	42.8	65.8
	ManiReg	✔	-	-	60.4 ± 0.8	67.2 ± 1.6	71.3 ± 1.4
Standard GNNs	GCN	✔	-	-	81.5 ± 1.3	71.9 ± 1.9	77.8 ± 2.9
	GAT	✔	-	-	83.0 ± 0.7	72.5 ± 0.7	79.0 ± 0.3
	SGC	-	-	-	81.0 ± 0.0	71.9 ± 0.1	78.9 ± 0.0
	GCN-kNN	✔	-	✔	72.2 ± 1.8	56.8 ± 3.2	74.5 ± 3.2
	GAT-kNN	✔	-	✔	73.8 ± 1.7	56.4 ± 3.8	75.4 ± 1.3
	Dense GAT	✔	-	✔	78.5 ± 2.5	66.4 ± 1.5	66.4 ± 1.5
	LDS	✔	-	✔	$\mathbf{83.9 \pm 0.6}$	$\mathbf{74.8 \pm 0.3}$	out-of-memory
	GLCN	✔	-	✔	83.1 ± 0.5	72.5 ± 0.9	78.4 ± 1.5
Diffusion-based models	GRAND-l	-	✔	-	83.6 ± 1.0	73.4 ± 0.5	78.8 ± 1.7
	GRAND	✔	✔	✔	83.3 ± 1.3	74.1 ± 1.7	78.1 ± 2.1
	GRAND++	✔	✔	✔	82.2 ± 1.1	73.3 ± 0.9	78.1 ± 0.9
	GDC	✔	-	-	83.6 ± 0.2	73.4 ± 0.3	78.7 ± 0.4
	GraphHeat	✔	-	-	83.7	72.5	**80.5**
	DGC-Euler	-	-	-	83.3 ± 0.0	73.3 ± 0.1	80.3 ± 0.1
Ours	DIFFORMER-s	-	-	✔	$\mathbf{84.7 \pm 0.1}$	73.5 ± 0.3	$\mathbf{81.8 \pm 0.3}$
	DIFFORMER-a	-	-	✔	83.7 ± 0.6	$\mathbf{75.7 \pm 0.3}$	$\mathbf{80.5 \pm 1.2}$

5 EXPERIMENTS

We apply DIFFORMER to various tasks for evaluation: 1) graph-based node classification where an input graph is given as observation; 2) image and text classification without input graphs; 3) dynamics prediction that requires handling new unseen instances from test data, i.e., inductive learning. In each case, we compare a different (with some overlap) set of competing models that are closely associated with DIFFORMER and specifically designed for the particular task. Unless otherwise stated, for datasets where input graphs are available, we incorporate them for feature propagation as is defined by Eq. 11. Due to space limit, we defer details of datasets to Appendix F and the implementations to Appendix G. Also, we provide additional supporting empirical results in Appendix H.

5.1 SEMI-SUPERVISED NODE CLASSIFICATION BENCHMARKS

We test DIFFORMER on three citation networks `Cora`, `Citeseer` and `Pubmed`. Table 2 reports the testing accuracy. We compare with several sets of baselines linked with our model from different aspects. 1) Basic models: *MLP* and two classical graph-based SSL models Label Propagation (*LP*) (Zhu et al., 2003) and *ManiReg* (Belkin et al., 2006). 2) GNN models: *SGC* (Wu et al., 2019), *GCN* (Kipf & Welling, 2017), *GAT* (Velickovic et al., 2018), their variants *GCN-kNN*, *GAT-kNN* (operating on kNN graphs constructed from input features) and *Dense GAT* (with a densely connected graph replacing the input one), and two strong structure learning models LDS (Franceschi et al., 2019) and GLCN (Jiang et al., 2019a). 3) PDE graph models: the SOTA models *GRAND* (Chamberlain et al., 2021a) (with its linear variant GRAND-l) and *GRAND++* (Thorpe et al., 2022). 4) Diffusion-inspired GNN models: *GDC* (Klicpera et al., 2019), *GraphHeat* (Xu et al., 2020) and a recent work *DGC-Euler* (Wang et al., 2021). Table 2 shows that DIFFORMER achieves the best results on three datasets with significant improvements. Also, we notice that the simple diffusivity model DIFFORMER-s significantly exceeds the counterparts without non-linearity (SGC, GRAND-l and DGC-Euler) and even comes to the first on `Cora` and `Pubmed`. These results suggest that DIFFORMER can serve as a very competitive encoder backbone for node-level prediction that learns inter-instance interactions for generating informative representations and boosting downstream performance.

5.2 LARGE-SCALE NODE CLASSIFICATION GRAPHS

We also consider two large-scale graph datasets `ogbn-Proteins`, a multi-task protein-protein interaction network, and `Pokec`, a social network. Table 3 presents the results. Due to the dataset size (0.13M/1.63M nodes for two graphs) and scalability issues that many of the competitors in Table 2 as well as DIFFORMER-a would potentially experience, we only compare DIFFORMER-s

Table 3: Testing ROC-AUC for `Proteins` and Accuracy for `Pokec` on large-scale node classification datasets. $*$ denotes using mini-batch training on a Tesla V100 with 16GB memory.

Models	Proteins	Pokec
MLP	72.41 ± 0.10	60.15 ± 0.03
LP	74.73	52.73
SGC	49.03 ± 0.93	52.03 ± 0.84
GCN	74.22 ± 0.49*	62.31 ± 1.13*
GAT	**75.11 ± 1.45***	**65.57 ± 0.34***
DIFFORMER-s	**79.49 ± 0.44***	**69.24 ± 0.76***

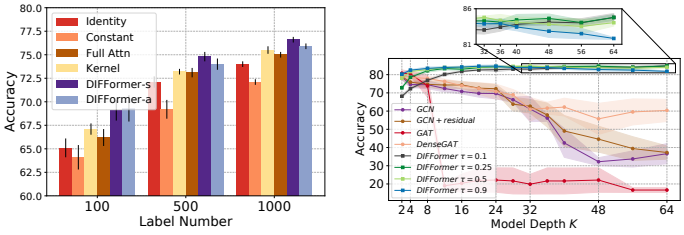

(a) (b)

Figure 2: (a) Ablation studies w.r.t. different diffusivity function forms on `CIFAR`. (b) Impact of K and τ on `Cora`.

Table 4: Testing accuracy for image (`CIFAR` and `STL`) and text (`20News`) classification.

Dataset		MLP	LP	ManiReg	GCN-kNN	GAT-kNN	DenseGAT	GLCN	DIFFORMER-s	DIFFORMER-a
CIFAR	100 labels	65.9 ± 1.3	66.2	67.0 ± 1.9	66.7 ± 1.5	66.0 ± 2.1	out-of-memory	66.6 ± 1.4	**69.1 ± 1.1**	**69.3 ± 1.4**
	500 labels	73.2 ± 0.4	70.6	72.6 ± 1.2	72.9 ± 0.4	72.4 ± 0.5	out-of-memory	72.8 ± 0.5	**74.8 ± 0.5**	**74.0 ± 0.6**
	1000 labels	75.4 ± 0.6	71.9	74.3 ± 0.4	74.7 ± 0.5	74.1 ± 0.5	out-of-memory	74.7 ± 0.3	**76.6 ± 0.3**	**75.9 ± 0.3**
STL	100 labels	66.2 ± 1.4	65.2	66.5 ± 1.9	**66.9 ± 0.5**	66.5 ± 0.8	out-of-memory	66.4 ± 0.8	**67.8 ± 1.1**	66.8 ± 1.1
	500 labels	**73.0 ± 0.8**	71.8	72.5 ± 0.5	72.1 ± 0.8	72.0 ± 0.8	out-of-memory	72.4 ± 1.3	**73.7 ± 0.6**	72.9 ± 0.7
	1000 labels	75.0 ± 0.8	72.7	74.2 ± 0.5	73.7 ± 0.4	73.9 ± 0.6	out-of-memory	74.3 ± 0.7	**76.4 ± 0.5**	**75.3 ± 0.6**
20News	1000 labels	54.1 ± 0.9	55.9	56.3 ± 1.2	56.1 ± 0.6	55.2 ± 0.8	54.6 ± 0.2	56.2 ± 0.8	**57.7 ± 0.3**	**57.9 ± 0.7**
	2000 labels	57.8 ± 0.9	57.6	60.0 ± 0.8	60.6 ± 1.3	59.1 ± 2.2	59.3 ± 1.4	60.2 ± 0.7	**61.2 ± 0.6**	**61.3 ± 1.0**
	4000 labels	62.4 ± 0.6	59.5	63.6 ± 0.7	64.3 ± 1.0	62.9 ± 0.7	62.4 ± 1.0	64.1 ± 0.8	**65.9 ± 0.8**	**64.8 ± 1.0**

with standard GNNs. In particular, we found GCN/GAT/DIFFORMER-s are still hard for full-graph training on a single V100 GPU with 16GM memory. We thus consider mini-batch training with batch size 10K/100K for `Proteins`/`Pokec`. We found that DIFFORMER outperforms common GNNs by a large margin, which suggests its desired efficacy on large datasets. As mentioned previously, we prioritize the efficacy of DIFFORMER as a general encoder backbone for solving node-level prediction tasks on large graphs. While there are quite a few practical tricks shown to be effective for training GNNs for this purpose, e.g., hop-wise attention (Sun et al., 2022) or various label re-use strategies, these efforts are largely orthogonal to our contribution here and can be applied to most any model to further boost performance. For further investigation, we supplement more results using different mini-batch sizes for training and study its impact on testing performance in Appendix H.4. Furthermore, we compare the training time and memory costs in Appendix H.5 where we found that DIFFORMER-s is about 6 times faster than GAT and 39 times faster than DenseGAT on `Pokec`, which suggests superior scalability and efficiency of DIFFORMER-s on large graphs.

5.3 IMAGE AND TEXT CLASSIFICATION WITH LOW LABEL RATES

We next conduct experiments on `CIFAR-10`, `STL-10` and `20News-Group` datasets to test DIFFORMER for standard classification tasks with limited label rates. For `20News` provided by Pedregosa et al. (2011), we take 10 topics and use words with TF-IDF more than 5 as features. For `CIFAR` and `STL`, two public image datasets, we first use the self-supervised approach SimCLR (Chen et al., 2020b) (that does not use labels for training) to train a ResNet-18 for extracting the feature maps as input features of instances. These datasets contain no graph structure, so we use kNN to construct a graph over input features for GNN competitors and do *not* use input graphs for DIFFORMER.

Table 4 reports the testing accuracy of DIFFORMER and competitors including MLP, ManiReg, GCN-kNN, GAT-kNN, DenseGAT and GLCN. Two DIFFORMER models perform much better than MLP in nearly all cases, suggesting the effectiveness of learning the inter-dependence over instances. Besides, DIFFORMER yields large improvements over GCN and GAT which are in some sense limited by the handcrafted graph that leads to sub-optimal propagation. Moreover, DIFFORMER significantly outperforms GLCN, a strong baseline that learns new (static) graph structures, which demonstrates the superiority of our evolving diffusivity that can adapt to different layers.

5.4 SPATIAL-TEMPORAL DYNAMICS PREDICTION

We consider three spatial-temporal datasets with details in Appendix F. Each dataset consists of a series of graph snapshots where nodes are treated as instances and each of them has a integer label (e.g., reported cases for `Chickenpox` or `Covid`). The task is to predict the labels of one

Table 5: Mean and standard deviation of MSE on spatial-temporal prediction datasets.

Dataset	MLP	GCN	GAT	Dense GAT	GAT-kNN	GCN-kNN	DIFFORMER-s	DIFFORMER-a	DIFFORMER-s w/o g	DIFFORMER-a w/o g
Chickenpox	0.924 (±0.001)	**0.923 (±0.001)**	0.924 (±0.002)	0.935 (±0.005)	0.926 (±0.004)	0.936 (±0.004)	0.926 (±0.002)	0.926 (±0.008)	**0.920 (±0.001)**	**0.920 (±0.002)**
Covid	0.956 (±0.198)	1.080 (±0.162)	1.052 (±0.336)	1.524 (±0.319)	0.861 (±0.123)	1.475 (±0.560)	**0.792 (±0.086)**	**0.792 (±0.076)**	**0.791 (±0.090)**	0.935 (±0.143)
WikiMath	1.073 (±0.042)	1.292 (±0.125)	1.339 (±0.073)	0.826 (±0.070)	0.882 (±0.015)	1.023 (±0.058)	0.922 (±0.015)	**0.738 (±0.031)**	0.993 (±0.042)	**0.720 (±0.036)**

snapshot based on the previous ones. Table 5 compares testing MSE of four DIFFORMER variants (here DIFFORMER-s w/o g denotes the model DIFFORMER-s without using input graphs) against baselines. We can see that two DIFFORMER variants without input graphs even outperform the counterparts using input structures in four out of six cases. This implies that our diffusivity estimation module could learn useful structures for informed prediction, and the input structure might not always contribute to positive effect. In fact, for temporal dynamics, the underlying relations that truly influence the trajectory evolution can be much complex and the observed relations could be unreliable with missing or noisy links, in which case GNN models relying on input graphs may perform undesirably. Compared to the competitors, our models rank the first with significant improvements.

5.5 FURTHER RESULTS AND DISCUSSIONS

How do different diffusivity functions perform? Figure 2(a) compares DIFFORMER with four variants using other diffusivity functions that have no essential connection with energy minimization: 1) *Identity* sets $\mathbf{S}^{(k)}$ as a fixed identity matrix; 2) *Constant* fixes $\mathbf{S}^{(k)}$ as all-one constant matrix; 3) *Full Attn* parameterizes $\mathbf{S}^{(k)}$ by attention networks (Vaswani et al., 2017); 4) *Kernel* adopts Gaussian kernel for computing $\mathbf{S}^{(k)}$. More results on other datasets are in Appendix H.1 and they consistently show that our adopted diffusivity forms produce superior performance, which verifies the effectiveness of our diffusivity designs derived from minimization of a principled energy.

How do model depth and step size impact the performance? We discuss the influence of model depth K and step size τ on `Cora` in Fig. 2(b). More results on `Citeseer` and `Pubmed` are generally consistent with Fig. 2(b) and deferred to Appendix H.2. The curves indicate that the performance of GCN and GAT models exhibit significant degradation with deeper layers, while DIFFORMER maintains its superiority and performs stably with large K. Furthermore, when K is not large enough (less than 32), there is a clear performance improvement of DIFFORMER as K increases, and larger τ contributes to a steeper increase. When K continues increasing (more than 32), the model performance still goes up with small τ (0.1 and 0.25) yet exhibits a slight drop with large τ (0.5 and 0.9). The reason could be that larger (smaller) τ contributes to more (less) concentration on global information from other instances in each iteration, which brings up more (less) benefits with increasing propagation layers yet could lead to instability when the step size is too large.

What is learned by the representation? We next try to shed some insights on how our diffusion models help to learn effective representations that facilitate downstream prediction, via visualizing node representations and layer-wise diffusivity strength in Appendix H.3. We found that the diffusivity strength estimates tend to increase the connectivity among nodes with different classes, and thus the updated node embeddings can absorb information from different communities for informative prediction. On the other hand, the produced representations exhibit smaller intra-class distance and larger inter-class distance, making them easier to be distinguished for classification. Comparing DIFFORMER-s and DIFFORMER-a on the temporal datasets, we found that DIFFORMER-s produces more concentrated large weights while DIFFORMER-a tends to have large diffusivity spreading out more and learn more complex structures. See more discussions in Appendix H.3.

6 CONCLUSIONS

This paper proposes an energy-driven geometric diffusion model with latent diffusivity function for data representations. The model encodes all the instances as a whole into evolving states aimed at minimizing a principled energy as implicit regularization. We further design two practical implementations with enough scalability and capacity for learning complex interactions over the underlying data geometry. Extensive experiments demonstrate the effectiveness and superiority of the model.

REFERENCES

James Atwood and Don Towsley. Diffusion-convolutional neural networks. In *Advances in neural information processing systems*, 2016.

Mikhail Belkin, Partha Niyogi, and Vikas Sindhwani. Manifold regularization: A geometric framework for learning from labeled and unlabeled examples. *Journal of machine learning research*, 7 (11), 2006.

Michael M. Bronstein, Joan Bruna, Yann LeCun, Arthur Szlam, and Pierre Vandergheynst. Geometric deep learning: going beyond euclidean data. *IEEE Signal Process. Mag*, 34:18–42, 2017.

Ben Chamberlain, James Rowbottom, Maria I. Gorinova, Michael M. Bronstein, Stefan Webb, and Emanuele Rossi. GRAND: graph neural diffusion. In *International Conference on Machine Learning (ICML)*, pp. 1407–1418, 2021a.

Benjamin Paul Chamberlain, James Rowbottom, Davide Eynard, Francesco Di Giovanni, Xiaowen Dong, and Michael M. Bronstein. Beltrami flow and neural diffusion on graphs. In *Advances in Neural Information Processing Systems (NeurIPS)*, 2021b.

Ming Chen, Zhewei Wei, Zengfeng Huang, Bolin Ding, and Yaliang Li. Simple and deep graph convolutional networks. In *International Conference on Machine Learning*, pp. 1725–1735, 2020a.

Ricky TQ Chen, Yulia Rubanova, Jesse Bettencourt, and David K Duvenaud. Neural ordinary differential equations. In *Advances in neural information processing systems*, 2018.

Ting Chen, Simon Kornblith, Mohammad Norouzi, and Geoffrey Hinton. A simple framework for contrastive learning of visual representations. In *International conference on machine learning*, pp. 1597–1607, 2020b.

Yu Chen, Lingfei Wu, and Mohammed J. Zaki. Iterative deep graph learning for graph neural networks: Better and robust node embeddings. In *Advances in Neural Information Processing Systems*, 2020c.

Vijay Prakash Dwivedi and Xavier Bresson. A generalization of transformer networks to graphs. *CoRR*, abs/2012.09699, 2020.

Bahare Fatemi, Layla El Asri, and Seyed Mehran Kazemi. Slaps: Self-supervision improves structure learning for graph neural networks. In *Advances in Neural Information Processing Systems*, 2021.

Luca Franceschi, Mathias Niepert, Massimiliano Pontil, and Xiao He. Learning discrete structures for graph neural networks. In *International Conference on Machine Learning*, pp. 1972–1982, 2019.

Mark I Freidlin and Alexander D Wentzell. Diffusion processes on graphs and the averaging principle. *The Annals of probability*, pp. 2215–2245, 1993.

Boumediene Hamzi and Houman Owhadi. Learning dynamical systems from data: A simple cross-validation perspective, part i: Parametric kernel flows. *Physica D: Nonlinear Phenomena*, 421: 132817, 2021.

Weihua Hu, Matthias Fey, Marinka Zitnik, Yuxiao Dong, Hongyu Ren, Bowen Liu, Michele Catasta, and Jure Leskovec. Open graph benchmark: Datasets for machine learning on graphs. In *Advances in Neural Information Processing Systems*, 2020.

Vassilis N. Ioannidis, Meng Ma, Athanasios N. Nikolakopoulos, and Georgios B. Giannakis. Kernel-based inference of functions over graphs. *CoRR*, abs/1711.10353, 2017.

Bo Jiang, Ziyan Zhang, Doudou Lin, Jin Tang, and Bin Luo. Semi-supervised learning with graph learning-convolutional networks. In *IEEE Conference on Computer Vision and Pattern Recognition*, pp. 11313–11320, 2019a.

Bo Jiang, Ziyan Zhang, Doudou Lin, Jin Tang, and Bin Luo. Semi-supervised learning with graph learning-convolutional networks. In *IEEE/CVF conference on computer vision and pattern recognition*, pp. 11313–11320, 2019b.

Thomas N. Kipf and Max Welling. Semi-supervised classification with graph convolutional networks. In *International Conference on Learning Representations (ICLR)*, 2017.

Johannes Klicpera, Stefan Weißenberger, and Stephan Günnemann. Diffusion improves graph learning. In *Advances in neural information processing systems*, 2019.

Isaac E Lagaris, Aristidis Likas, and Dimitrios I Fotiadis. Artificial neural networks for solving ordinary and partial differential equations. *IEEE transactions on neural networks*, 9(5):987–1000, 1998.

Georgi S Medvedev. The nonlinear heat equation on dense graphs and graph limits. *SIAM Journal on Mathematical Analysis*, 46(4):2743–2766, 2014.

Fabian Pedregosa, Gaël Varoquaux, Alexandre Gramfort, Vincent Michel, Bertrand Thirion, Olivier Grisel, Mathieu Blondel, Peter Prettenhofer, Ron Weiss, Vincent Dubourg, et al. Scikit-learn: Machine learning in python. *the Journal of machine Learning research*, 12:2825–2830, 2011.

R. T Rockafellar. Convex analysis. *Princeton University Press*, 1970.

Steven Rosenberg and Rosenberg Steven. *The Laplacian on a Riemannian manifold: an introduction to analysis on manifolds*. Number 31. Cambridge University Press, 1997.

Benedek Rozemberczki, Paul Scherer, Yixuan He, George Panagopoulos, Alexander Riedel, Maria Astefanoaei, Oliver Kiss, Ferenc Beres, Guzmán López, Nicolas Collignon, et al. Pytorch geometric temporal: Spatiotemporal signal processing with neural machine learning models. In *Proceedings of the 30th ACM International Conference on Information & Knowledge Management*, pp. 4564–4573, 2021.

Franco Scarselli, Marco Gori, Ah Chung Tsoi, Markus Hagenbuchner, and Gabriele Monfardini. The graph neural network model. *IEEE transactions on neural networks*, 20(1):61–80, 2008.

Prithviraj Sen, Galileo Namata, Mustafa Bilgic, Lise Getoor, Brian Gallagher, and Tina Eliassi-Rad. Collective classification in network data. *AI Mag.*, 29(3):93–106, 2008.

Chuxiong Sun, Jie Hu, Hongming Gu, Jinpeng Chen, and Mingchuan Yang. Adaptive graph diffusion networks. *CoRR*, abs/2012.15024, 2022.

Matthew Thorpe, Hedi Xia, Tan Nguyen, Thomas Strohmer, Andrea L. Bertozzi, Stanley J. Osher, and Bao Wang. GRAND++: graph neural diffusion with a source term. In *International Conference on Learning Representations (ICLR)*, 2022.

Anton Tsitsulin, Davide Mottin, Panagiotis Karras, Alexander M. Bronstein, and Emmanuel Müller. Netlsd: Hearing the shape of a graph. In *ACM SIGKDD International Conference on Knowledge Discovery & Data Mining*, pp. 2347–2356, 2018.

Ashish Vaswani, Noam Shazeer, Niki Parmar, Jakob Uszkoreit, Llion Jones, Aidan N. Gomez, Lukasz Kaiser, and Illia Polosukhin. Attention is all you need. In *Advances in Neural Information Processing Systems*, pp. 5998–6008, 2017.

Petar Velickovic, Guillem Cucurull, Arantxa Casanova, Adriana Romero, Pietro Liò, and Yoshua Bengio. Graph attention networks. In *International Conference on Learning Representations (ICLR)*, 2018.

Yifei Wang, Yisen Wang, Jiansheng Yang, and Zhouchen Lin. Dissecting the diffusion process in linear graph convolutional networks. In *Advances in Neural Information Processing Systems*, 2021.

Yue Wang, Yongbin Sun, Ziwei Liu, Sanjay E. Sarma, Michael M. Bronstein, and Justin M. Solomon. Dynamic graph CNN for learning on point clouds. *ACM Trans. Graph.*, 38(5):146:1–146:12, 2019.

Jason Weston, Frédéric Ratle, Hossein Mobahi, and Ronan Collobert. Deep learning via semi-supervised embedding. In *Neural networks: Tricks of the trade*, pp. 639–655. Springer, 2012.

Felix Wu, Amauri H. Souza Jr., Tianyi Zhang, Christopher Fifty, Tao Yu, and Kilian Q. Weinberger. Simplifying graph convolutional networks. In *International Conference on Machine Learning*, pp. 6861–6871, 2019.

Bingbing Xu, Huawei Shen, Qi Cao, Keting Cen, and Xueqi Cheng. Graph convolutional networks using heat kernel for semi-supervised learning. *arXiv preprint arXiv:2007.16002*, 2020.

Yongyi Yang, Tang Liu, Yangkun Wang, Jinjing Zhou, Quan Gan, Zhewei Wei, Zheng Zhang, Zengfeng Huang, and David Wipf. Graph neural networks inspired by classical iterative algorithms. In *International Conference on Machine Learning*, pp. 11773–11783, 2021.

Zhilin Yang, William W. Cohen, and Ruslan Salakhutdinov. Revisiting semi-supervised learning with graph embeddings. In *International Conference on Machine Learning (ICML)*, pp. 40–48, 2016.

Yingxue Zhang, Soumyasundar Pal, Mark Coates, and Deniz Üstebay. Bayesian graph convolutional neural networks for semi-supervised classification. In *AAAI Conference on Artificial Intelligence*, pp. 5829–5836, 2019.

Dengyong Zhou, Olivier Bousquet, Thomas Navin Lal, Jason Weston, and Bernhard Schölkopf. Learning with local and global consistency. In *Advances in Neural Information Processing Systems*, pp. 321–328, 2004.

Xiaojin Zhu, Zoubin Ghahramani, and John D. Lafferty. Semi-supervised learning using gaussian fields and harmonic functions. In *International Conference on Machine Learning (ICML)*, pp. 912–919, 2003.

A PROOF FOR THEOREM 1

First of all, we can convert the minimization of Eq. 4 into a minimization of its variational upper bound, shown in the following proposition.

Proposition 1. *The energy function $E(\mathbf{Z}, k; \delta)$ is upper bounded by*

$$\tilde{E}(\mathbf{Z}, k; \{\omega_{ij}\}, \tilde{\delta}) = \|\mathbf{Z} - \mathbf{Z}(k)\|_{\mathcal{F}}^2 + \lambda \left[\sum_{i,j} \omega_{ij} \|\mathbf{z}_i - \mathbf{z}_j\|_2^2 - \tilde{\delta}(\omega_{ij}) \right], \tag{12}$$

where $\tilde{\delta}$ is the concave conjugate of δ, and the equality holds if and only if the variational parameters satisfy

$$\omega_{ij} = \left. \frac{\partial \delta(z^2)}{\partial z^2} \right|_{z = \|\mathbf{z}_i - \mathbf{z}_j\|_2}. \tag{13}$$

Proof. The proof of the proposition follows the principles of convex analysis and Fenchel duality (Rockafellar, 1970). For any concave and non-decreasing function $\rho : \mathbb{R}^+ \to \mathbb{R}$, one can express it as the variational decomposition

$$\rho(z^2) = \min_{\omega \geq 0} [\omega z^2 - \tilde{\rho}(\omega)] \geq \omega z^2 - \tilde{\rho}(\omega), \tag{14}$$

where ω is a variational parameter and $\tilde{\rho}$ is the concave conjugate of ρ. Eq. 14 essentially defines $\rho(z^2)$ as the minimal envelope of a series of quadratic bounds $\omega z^2 - \tilde{\rho}(\omega)$ defined by a different values of $\omega \geq 0$ and the upper bound is given for a fixed ω when removing the minimization operator. Based on this, we obtain the result of Eq. 12. In terms of the sufficient and necessary condition for equality, we note that for any optimal ω^* we have

$$\omega^* z^2 - \tilde{\rho}(\omega^*) = \rho(z^2), \tag{15}$$

which is tangent to ρ at z^2 and $\omega^* = \frac{\partial \delta(z^2)}{\partial z^2}$. We thus obtain the result of Eq. 13. □

We next continue to prove the main result of Theorem 1. According to Proposition 1, we can minimize the upper bound surrogate Eq. 12 and it becomes equivalent to a minimization of the original energy on condition that the variational parameters are given by Eq. 13. Then with a one-step gradient decent of Eq. 12, the instance states could be updated via (assuming l as the index of steps and α as step size)

$$\begin{aligned} \mathbf{Z}^{(l+1)} &= \mathbf{Z}^{(l)} - \alpha \left. \frac{\partial \tilde{E}(\mathbf{Z}; \delta)}{\partial \mathbf{Z}} \right|_{\mathbf{Z} = \mathbf{Z}^{(l)}} \\ &= \mathbf{Z}^{(l)} - \alpha \left(\lambda (\mathbf{D}^{(l)} - \mathbf{\Omega}^{(l)}) \mathbf{Z}^{(l)} + \mathbf{Z}^{(l)} - \mathbf{Z}^{(l)} \right) \\ &= \mathbf{Z}^{(l)} - \alpha' (\mathbf{D}^{(l)} - \mathbf{\Omega}^{(l)}) \mathbf{Z}^{(l)} \end{aligned} \tag{16}$$

where $\mathbf{\Omega}^{(l)} = \{\omega_{ij}^{(l)}\}_{N \times N}$, $\mathbf{D}^{(l)}$ denotes the diagonal degree matrix associated with $\mathbf{\Omega}^{(l)}$ and we introduce $\alpha' = \alpha\lambda$ to combine two parameters as one. Common practice to accelerate convergence adopts a positive definite preconditioner term, e.g., $(\mathbf{D}^{(l)})^{-1}$, to re-scale the updating gradient and the final updating form becomes

$$\mathbf{Z}^{(l+1)} = (1 - \alpha') \mathbf{Z}^{(l)} + \alpha' (\mathbf{D}^{(l)})^{-1} \mathbf{\Omega}^{(l)} \mathbf{Z}^{(l)}. \tag{17}$$

One can notice that Eq. 17 shares similar forms as the numerical iteration Eq. 3 for the PDE diffusion system, in particular if we write Eq. 3 as a matrix form:

$$\mathbf{Z}^{(k+1)} = \left(1 - \tau \tilde{\mathbf{D}}^{(k)} \right) \mathbf{Z}^{(k)} + \tau \mathbf{S}^{(k)} \mathbf{Z}^{(k)}. \tag{18}$$

where $\tilde{\mathbf{D}}^{(k)}$ is the degree matrix associated with $\mathbf{S}^{(k)}$. Pushing further, we can see that the effect of Eq. 18 is the same as 17 when we let $\tau = \alpha'$, $k = l$, $\mathbf{S}^{(k)} = (\mathbf{D}^{(l)})^{-1} \mathbf{\Omega}^{(l)}$ and $\mathbf{S}^{(k)}$ is row-normalized, i.e., $\sum_{v \in V} \mathbf{S}_{uv}^{(k)} = 1$ and $\tilde{\mathbf{D}}^{(k)} = \mathbf{I}$.

Thereby, we have proven by construction that a one-step numerical iteration by the explicit Euler scheme, specifically shown by Eq. 17 is equivalent to a one-step gradient descent on the surrogate Eq. 14 which further equals to the original energy Eq. 4. We thus have the result $E(\mathbf{Z}^{(k+1)}, k; \delta) \leq E(\mathbf{Z}^{(k)}, k; \delta)$. Besides, we notice that for a fixed $\mathbf{Z}$, $E(\mathbf{Z}, k; \delta) = \|\mathbf{Z} - \mathbf{Z}^{(k)}\|_{\mathcal{F}}^2 + \lambda \sum_{ij} \rho(\|\mathbf{z}_i - \mathbf{z}_j\|_2^2)$ becomes a function of k and its optimum is achieved if and only if $\mathbf{Z}^{(k)} = \mathbf{Z}$. Such a fact yields that $E(\mathbf{Z}^{(k)}, k; \delta) \leq E(\mathbf{Z}^{(k)}, k-1; \delta)$. The result of the main theorem follows by noting that $E(\mathbf{Z}^{(k+1)}, k; \delta) \leq E(\mathbf{Z}^{(k)}, k; \delta) \leq E(\mathbf{Z}^{(k)}, k-1; \delta)$.

B Extension of our Theory to Incorporate Non-Linearity

In Section 3, we mainly focus on the situation without non-linearity in each model layer to stay consistent with our implementation where we empirically found that omitting the non-linearity in the middle diffusion layers works smoothly in practice (see the pseudo code of Alg. 1 in appendix for details). Even so, our theory can also be extended to incorporate the layer-wise non-linearity in diffusion propagation. Specifically, the non-linear activation can be treated as a proximal operator (which projects the output into a feasible region) and the gradient descent used in our analysis Eqn. 16 and 17 can be modified to add a proximal operator:

$$\mathbf{Z}^{(l+1)} = \mathrm{Prox}_{\Omega}\left((1-\alpha)\mathbf{Z}^{(l)} + \alpha(\mathbf{D}^{(l)})^{-1}\mathbf{\Omega}^{(l)}\mathbf{Z}^{(l)}\right),$$

where $\mathrm{Prox}_{\Omega}(z) = \arg\min_{x \in \Omega} \|x - z\|_2$ and Ω defines a feasible region. The updating above corresponds to proximial gradient descent which also guarantees a strict minimization for the energy function and our Theorem 1 will still hold. In particular, if one uses ReLU activation, the proximal operator will be $\mathrm{Prox}_{\Omega}(z) = \max(0, z)$.

C Different Energy Forms

We present more detailed illustration for the choices of f associated with specific energy function forms in Eq. 4.

Simple Diffusivity Model. As discussed in Section 4, the simple model assumes $f(z^2) = 2 - \frac{1}{2}z^2$ that corresponds to $g(x) = 1 + x$, where we define $z = \|\mathbf{z}_i - \mathbf{z}_j\|_2$ and $x = \mathbf{z}_i^\top \mathbf{z}_j$. We plot the penalty function curves in Fig. 3(a). As we can see, the f is a non-negative, decreasing function of z^2, which implies that the δ satisfies the non-decreasing and concavity properties to guarantee a valid regularized energy function. Also, in Fig. 3(a) we present the divergence field produced by 10 randomly generated instances (marked as red stars) and the cross-section energy field of one instance.

Advanced Diffusivity Model. The diffusivity model defines $f(z^2) = \frac{1}{1+e^{z^2/2-1}}$ with $g(x) = \frac{1}{1+\exp(-x)}$. The penalty function curves, divergence field and energy field are shown in Fig. 3(b).

Incorporating Input Graphs. In Section 4, we present an extended version of our model for incorporating input graphs. Such an extension defines a new diffusion process whose iterations can be intrinsically viewed as a minimization for the following regularized energy:

$$E(\mathbf{Z}, k; \delta) = \|\mathbf{Z} - \mathbf{Z}^{(k)}\|_{\mathcal{F}}^2 + \frac{\lambda}{2}\sum_{i,j}\delta(\|\mathbf{z}_i - \mathbf{z}_j\|_2^2) + \frac{\lambda}{2}\sum_{(i,j)\in\mathcal{E}}\|\mathbf{z}_i - \mathbf{z}_j\|_2^2, \tag{19}$$

where the last term is a penalty for observed edges in the input graph.

D Model Implementation and Pseudo Codes

In this section, we present the details for model implementation including the feed-forward and loss computation of DIFFormer (shown in Alg. 1) and the one-layer computation of two model versions (shown in Alg. 2 for DIFFormer-s and Alg. 3 for DIFFormer-a). The key design of our methodology lies in the model architectures which are shown in detail in Alg. 2 for DIFFormer-s and Alg. 3 for DIFFormer-a, where for each case, the model takes the data as input and outputs prediction for each individual instance. For more details concerning the implementation, please refer to our provided codes in the supplementary.

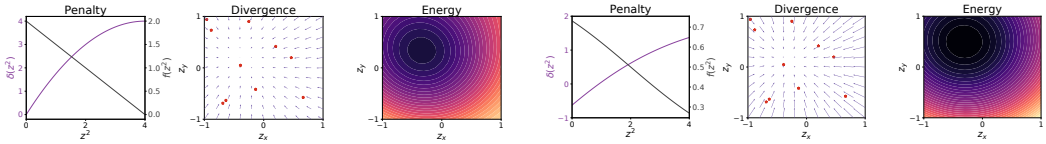

(a) DIFFORMER-s: $\delta(z^2) = 2z^2 - \frac{1}{4}z^4$ (b) DIFFORMER-a: $\delta(z^2) = z^2 - 2\log(e^{z^2/2-1} + 1)$

Figure 3: Plot of penalty curves $\delta(z^2)$ and $f(z^2) = \frac{\partial \delta(z^2)}{\partial z^2}$, divergence field (produced by 10 randomly generated instances marked as red stars) and cross-section energy field of an individual.

Algorithm 1 PyTorch-style Code for DIFFORMER

```
# fcs: fully-connected layers
# bns: layer normalization layers
# convs: endiff layers (see implementation in Alg. 2 and 3)
# activation: activation function for the input layer
# x: input data sized [N, D], N for instance number, D for input feature dimension
# edge_index: input graph structure if available, None otherwise
# tau: step size for each iteration update

layer_ = []

# input MLP layer
x = fcs[0](x)
x = bns[0](x)
x = activation(x)

# store as residual link
layer_.append(x)

for i, conv in enumerate(convs):
   # graph convolution with full attention aggregation
   x = conv(x, x, edge_index)
   x = tau * x + (1-tau) * layer_[i]
   x = bns[i+1](x)
   layer_.append(x)

# output MLP layer
out = fcs[-1](x)

# supervised loss calculation, negative log-likelihood
y_logp = F.log_softmax(out, dim=1)
loss = criterion(y_logp[train_idx], y_true[train_idx])
```

Algorithm 2 PyTorch-style Code for One-layer Feed-forward of DIFFORMER-s

```
# x: data embeddings sized [N, d], N for instance number, d for hidden size
# edge_index: input graph structure if available, None otherwise
# H: head number
# use_graph: whether to use input graph
# use_weight: whether to use feature transformation for each layer
# graph_conv: graph convolution operatior using the normalized adjacency matrix D^{-1/2}
    AD^{-1/2}
# Wq, Wk, Wv: weight matrices for feature transformation

q = Wq(x)
k = Wk(x)
v = use_weight * Wv(x) + (1 - use_weight) * x

# numerator
kv = torch.einsum("lhm,lhd->hmd", k, v)
num = torch.einsum("nhm,hmd->nhd", q, kv) # [N, H, D]
num += N * v

# denominator
all_ones = torch.ones(N)
k_sum = torch.einsum("lhm,l->hm", k, all_ones)
den = torch.einsum("nhm,hm->nh", q, k_sum) # [N, H]

# aggregated results
den += torch.ones_like(den) * N
agg = num / den.unsqueeze(2) # [N, H, D]

# use input graph for graph conv
if use_graph:
   agg = agg + graph_conv(v, edge_index)
output = agg.mean(dim=1)
```

Algorithm 3 PyTorch-style Code for One-layer Feed-forward of DIFFORMER-a

```
# x: data embeddings sized [N, d], N for instance number, d for hidden size
# edge_index: input graph structure if available, None otherwise
# H: head number
# use_graph: whether to use input graph
# use_weight: whether to use feature transformation for each layer
# graph_conv: graph convolution operatior using the normalized adjacency matrix D^{-1/2}
    AD^{-1/2}
# Wq, Wk, Wv: weight matrices for feature transformation

q = Wq(x)
k = Wk(x)
v = use_weight * Wv(x) + (1 - use_weight) * x

# numerator
num = torch.sigmoid(torch.einsum("nhm,lhm->nlh", q, k)) # [N, N, H]

# denominator
all_ones = torch.ones(N)
den = torch.einsum("nlh,l->nh", num, all_ones)
den = den.unsqueeze(1).repeat(1, N, 1) # [N, N, H]

# aggregated results
attn = num / den
agg = torch.einsum("nlh,lhd->nhd", attn, v) # [N, H, D]

# use input graph for graph conv
if use_graph:
   agg = agg + graph_conv(v, edge_index)
output = agg.mean(dim=1)
```

E CONNECTIONS WITH EXISTING MODELS

MLP. MLPs can be viewed as a simplified diffusion model with only non-zero diffusivity values on the diagonal line, i.e., $\mathbf{S}_{ij}^{(k)} = 1$ if $i = j$ and 0 otherwise. From a graph convolution perspective, MLP only considers propagation on the self-loop connection in each layer. Correspondlying, the energy function the feed-forward process of the model essentially optimizes would be $E(\mathbf{Z}, k) = \|\mathbf{Z} - \mathbf{Z}^{(k)}\|_{\mathcal{F}}^2$, which only counts for the local consistency term and ignores the global information.

GCN. Graph Convolution Networks (Kipf & Welling, 2017) define a convolution operator on a graph $\mathcal{G} = (\mathcal{V}, \mathcal{E})$ by multiplying the node feature matrix with $D^{-\frac{1}{2}}AD^{-\frac{1}{2}}$ where A denotes the adjacency matrix and D is its associated degree matrix. The layer-wise updating rule can be written as

$$\begin{aligned} \hat{\mathbf{S}}_{ij}^{(k)} &= \begin{cases} \dfrac{1}{\sqrt{d_i d_j}}, & \text{if } (i,j) \in \mathcal{E}, \\ 0, & otherwise, \end{cases} \\ \mathbf{z}_i^{(k+1)} &= \left(1 - \tau \sum_{j=1}^{N} \hat{\mathbf{S}}_{ij}^{(k)}\right) \mathbf{z}_i^{(k)} + \tau \sum_{j=1}^{N} \hat{\mathbf{S}}_{ij}^{(k)} \mathbf{z}_j^{(k)}, \quad 1 \le i \le N. \end{aligned} \tag{20}$$

Eq. 20 generalizes the original message-passing rule of GCN by adding an additional self-loop links with adaptive weights for different nodes. The diffusivity matrix is defined with the observed adjacency, i.e., $\hat{\mathbf{S}}^{(k)} = D^{-\frac{1}{2}}AD^{-\frac{1}{2}}$. Though such a design leverages the geometric information from input structures as a guidance for feature propagation, it constrains the efficiency of layer-wise information flows within the receptive field of local neighbors and could only exploit partial global information with a finite number of iterations.

GAT. Graph Attention Networks (Velickovic et al., 2018) extend the GCN architecture to incorporate attention mechanisms as a learnable function producing adaptive weights for each observed edge. From our diffusion perspective, the attention matrix for layer-wise convolution can be treated as the

diffusivity in our updating rule:

$$\begin{aligned}\hat{\mathbf{S}}_{ij}^{(k)} &= \frac{f(\|\mathbf{z}_i^{(k)} - \mathbf{z}_j^{(k)}\|_2^2)}{\sum_{(i,l)\in\mathcal{E}} f(\|\mathbf{z}_i^{(k)} - \mathbf{z}_l^{(k)}\|_2^2)}, \quad (i,j) \in \mathcal{E}, \\ \mathbf{z}_i^{(k+1)} &= \left(1 - \tau \sum_{j=1}^{N} \hat{\mathbf{S}}_{ij}^{(k)}\right) \mathbf{z}_i^{(k)} + \tau \sum_{j=1}^{N} \hat{\mathbf{S}}_{ij}^{(k)} \mathbf{z}_j^{(k)}, \quad 1 \le i \le N.\end{aligned} \tag{21}$$

We notice that $\sum_{j=1}^{N} \hat{\mathbf{S}}_{ij}^{(k)} = 1$ due to the normalization in the denominator. Therefore, the layer-wise updating can be viewed as an attentive aggregation over graph structures and a subsequent residual link. In fact, the original implementation for the GAT model (Velickovic et al., 2018) specifies the function f as a particular form, i.e., $\exp(\text{LeakyReLU}(\mathbf{a}^\top[\mathbf{W}\mathbf{z}_i^{(k)} \| \mathbf{W}\mathbf{z}_j^{(k)}]))$, which can be viewed as a generalized similarity function given trainable $\mathbf{W}$, $\mathbf{a}$ towards optimizing a supervised loss.

F Dataset Information

In this section, we present the detailed information for all the experimental datasets, the pre-processing and evaluation protocol used in Section 5.

Table 6: Information for node classification datasets.

Dataset	Type	# Nodes	# Edges	# Node features	# Class
Cora	Citation network	2,708	5,429	1,433	7
Citeseer	Citation network	3,327	4,732	3,703	6
Pubmed	Citation network	19,717	44,338	500	3
Proteins	Protein interaction	132,534	39,561,252	8	2
Pokec	Social network	1,632,803	30,622,564	65	2

F.1 Node Classification Datasets

`Cora`, `Citeseer` and `Pubmed` (Sen et al., 2008) are commonly used citation networks for evaluating models on node classification tasks., These datasets are small-scale networks (with 2K∼20K nodes) and the goal is to classify the topics of documents (instances) based on input features of each instance (bag-of-words representation of documents) and graph structure (citation links). Following the semi-supervised learning setting in Kipf & Welling (2017), we randomly choosing 20 instances per class for training, 500/1000 instances for validation/testing for each dataset. `OGBN-Proteins` (Hu et al., 2020) is a multi-task protein-protein interaction network whose goal is to predict molecule instances' property. We follow the original splitting of Hu et al. (2020) for evaluation. `Pokec` is a large-scale social network with features including profile information, such as geographical region, registration time, and age, for prediction on users' gender. For semi-supervised learning, we consider randomly splitting the instances into train/valid/test with 10%/10%/80% ratios. Table 6 summarizes the statistics of these datasets.

F.2 Image and Text Classification Datasets

We evaluate our model on two image classification datasets: STL-10 and CIFAR-10. We use all 13000 images from STL-10, each of which belongs to one of ten classes. We choose 1500 images from each of 10 classes of CIFAR-10 and obtain a total of 15,000 images. For STL-10 and CIFAR-10, we randomly select 10/50/100 instances per class as training set, 1000 instances for validation and the remaining instances for testing. We first use the self-supervised approach SimCLR (Chen et al., 2020b) (that does not use labels for training) to train a ResNet-18 for extracting the feature maps as input features of instances. We also evaluate our model on 20Newsgroup, which is a text classification dataset consisting of 9607 instances. We follow Franceschi et al. (2019) to take 10 classes from 20 Newsgroup and use words (TFIDF) with a frequency of more than 5% as features.

F.3 SPATIAL-TEMPORAL DATASETS

The spatial-temporal datasets are from the open-source library PyTorch Geometric Temporal (Rozemberczki et al., 2021), with properties and summary statistics described in Table 7. Node features are evolving for all the datasets considered here, i.e., we have different node features for different snapshots. For each dataset, we split the snapshots into training, validation, and test sets according to a 2:2:6 ratio in order to make it more challenging and close to the real-world low-data learning setting. In details:

- `Chickenpox` describes weekly officially reported cases of chickenpox in Hungary from 2005 to 2015, whose nodes are counties and edges denote direct neighborhood relationships. Node features are lagged weekly counts of the chickenpox cases (we included 4 lags). The target is the weekly number of cases for the upcoming week (signed integers).
- `Covid` contains daily mobility graph between regions in England NUTS3 regions, with node features corresponding to the number of confirmed COVID-19 cases in the previous days from March to May 2020. The graph indicates how many people moved from one region to the other each day, based on Facebook Data For Good disease prevention maps. Node features correspond to the number of COVID-19 cases in the region in the past 8 days. The task is to predict the number of cases in each node after 1 day.
- `WikiMath` is a dataset whose nodes describe Wikipedia pages on popular mathematics topics and edges denote the links from one page to another. Node features are provided by the number of daily visits between 2019 March and 2021 March. The graph is directed and weighted. Weights represent the number of links found at the source Wikipedia page linking to the target Wikipedia page. The target is the daily user visits to the Wikipedia pages between March 16th 2019 and March 15th 2021 which results in 731 periods.

Table 7: Properties and summary statistics of the spatial-temporal datasets used in the experiments with information about whether the graph structure is dynamic or static, meaning of node features (the same as the prediction target) and the corresponding dimension (D), the number of snapshots (T), the number of nodes ($|V|$), as well as the meaning of edges/edge weights.

Dataset	Graph structure	Node features/ Target	D	Frequency	T	$\lvert V\rvert$	Edges/ Edge weights
Chickenpox	Static	Weekly Chickenpox Cases	4	Weekly	522	20	Direct Neighborhoods
Covid	Dynamic	Daily Covid Cases	8	Daily	61	129	Daily Mobility
WikiMath	Static	Daily User Visits	14	Daily	731	1,068	Page Links

G IMPLEMENTATION DETAILS AND HYPER-PARAMETERS

G.1 NODE CLASSIFICATION EXPERIMENT

We use feature transformation for each layer on two large datasets and omit it for citation networks. The head number is set as 1. We set $\tau = 0.5$ and incorporate the input graphs for DIFFORMER. For other hyper-paramters, we adopt grid search for all the models with learning rate from $\{0.0001, 0.001, 0.01, 0.1\}$, weight decay for the Adam optimizer from $\{0, 0.0001, 0.001, 0.01, 0.1, 1.0\}$, dropout rate from $\{0, 0.2, 0.5\}$, hidden size from $\{16, 32, 64\}$, number of layers from $\{2, 4, 8, 16, 32, 64\}$. For evaluation, we compute the mean and standard deviation of the results with five repeating runs with different initializations. For each run, we run for a maximum of 1000 epochs and report the testing performance achieved by the epoch yielding the best performance on validation set.

G.2 IMAGE AND TEXT CLASSIFICATION EXPERIMENT

For image and text datasets, we consider feature transformation for layer-wise updating. The head number is set as 1. We set $\tau = 0.5$. These datasets do not have input graphs so we only consider learning new structures for the diffusion model. For hyper-parameter settings, we conduct grid search for all the models with learning rate from $\{0.0001, 0.0005, 0.005, 0.01, 0.05\}$, weight decay for the Adam optimizer from $\{0.0001, 0.001, 0.01, 0.1\}$, dropout rate from $\{0, 0.2, 0.5\}$, hidden size from

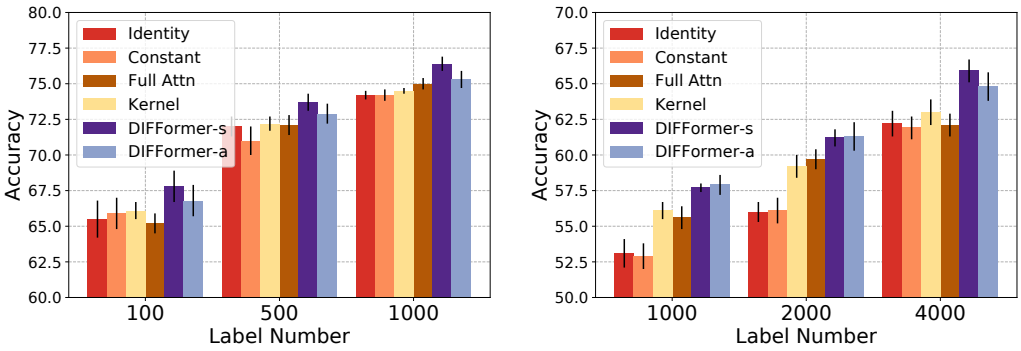

(a) STL (b) 20News

Figure 4: Ablation studies for different energy function forms on image and text datasets.

$\{32, 64, 100, 200, 300, 400\}$, number of layers from $\{1, 2, 4, 6, 8, 10, 12\}$. We average the results for five repeating runs and report as well the standard deviation. For each run, we run for a maximum of 600 epochs and report the testing accuracy achieved by the epoch yielding the highest accuracy on validation set.

G.3 Spatial-Temporal Prediction Experiment

We do not use feature transformation for these datasets due to their small sizes and also set $\tau = 0.5$. The head number is set as 1. These spatial-temporal dynamics prediction datasets contain available graph structures, we consider both cases, using the input graphs and not, in our experiments and discuss their impact on the performance. For other hyper-parameters, we also consider grid search for all models here with learning rate from $\{0.01, 0.05, 0.005\}$, weight decay for the Adam optimizer from $\{0, 0.005\}$, dropout rate from $\{0, 0.2, 0.5\}$, and report the test mean squared error (MSE) based on the lowest validation MSE. We average the results for five repeating runs and report as well the standard deviation for each MSE result. For each run, we run for a maximum of 200 epochs in total and stop the training process with 20-epoch early stopping on the validation performance. The data split is done in time order, and hence is deterministic. We report the results using the same hidden size (4) and number of layers (2) for all methods.

H More Experiment Results

We supplement more experiment results including extra ablation studies, hyper-parameter studies and visualization results on more datasets that are not presented in Section 5 due to the limit of space.

H.1 Ablation Studies

In Fig. 4 we present more experiment results for ablation studies w.r.t. the energy function forms used by DIFFormer. See discussions and analysis in Section 5.

H.2 Hyper-parameter Analysis

We plot the testing performance of several baselines and DIFFormer with different step size τ as the model size K increases in Fig. 5. See discussions and analysis in Section 5.

H.3 Visualization

Fig. 6 and 7 plot the produced instance-level representations and diffusion strength estimates by the model on 20News and STL, respectively. We observe that the diffusivity estimates tend to connect nodes with different classes, which contribute to increasing the global connectivity and facilitate

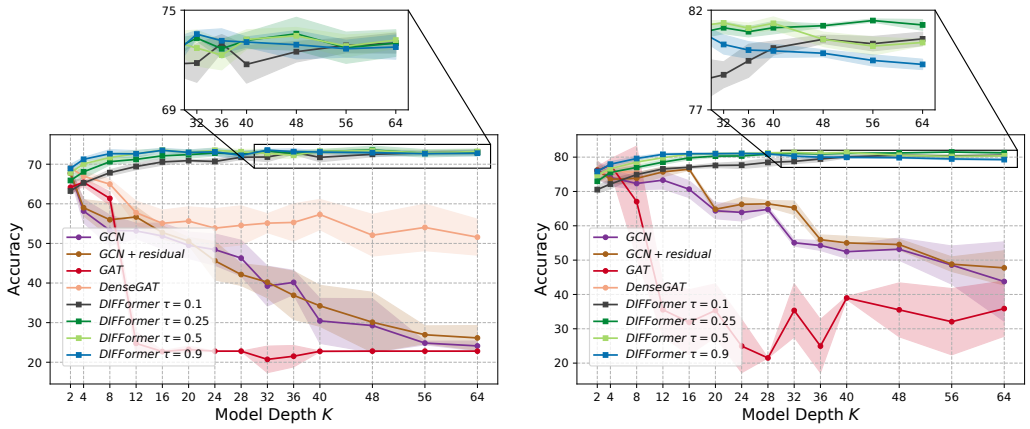

(a) Citeseer (b) Pubmed

Figure 5: Hyper-parameter studies of model depth K and step size τ on two citation networks.

absorbing other instances' information for informative representations. The node embeddings produced by our model have small intra-class distance and large inter-class distance, making it easier for the classifier to distinguish.

Fig. 8 visualizes the diffusivity estimates on Chickenpox. We conclude that large diffusion strength usually exists between nodes with similar ground-truth labels. DIFFORMER-s has more concentrated large weights while DIFFORMER-a tends to have large diffusivity spreading out more. DIFFORMER-a indeed learns more complex underlying structures than DIFFORMER-s due to its better capacity for diffusivity modeling.

H.4 IMPACT OF MINI-BATCH SIZES ON LARGE GRAPHS

The randomness of mini-batch partition on large graphs has negligible effect on the performance since we use large batch sizes for training, which is facilitated by the linear complexity of DIFFORMER-s. Even setting the batch size to be 100000, our model only costs 3GB GPU memory on Pokec. As a further investigation on this, we add more experiments using different batch sizes on Pokec and the results are shown in Table 8.

Table 8: Discussions on using different mini-batch sizes for training on Pokec. We report testing accuracy and training memory for comparison.

Batch size	5000	10000	20000	50000	100000	200000
Test Acc (%)	65.24 ± 0.34	67.48 ± 0.81	68.53 ± 0.75	68.96 ± 0.63	69.24 ± 0.76	69.15 ± 0.52
GPU Memory (MB)	1244	1326	1539	2060	2928	4011

One can see that using small batch sizes would indeed sacrifice the performance yet large batch sizes can produce decent and low-variance results with acceptable memory costs.

H.5 COMPARISON OF RUNNING TIME AND MEMORY COSTS

To further study the efficiency and scalability of our model, we provide more comparison regarding the training time per epoch and memory costs of DIFFORMER, GCN, GAT and DenseGAT in Table 9.

One can see that compared to GAT, DIFFORMER-s costs comparable time on small dataset Cora and is much faster on large dataset Pokec. As for memory consumption, DIFFORMER-s reduces the costs by several times over DenseGAT, which clearly shows the efficiency of our new diffusion function designs. Overall, DIFFORMER-s has nice scalability, decent efficiency and yield significantly better accuracy.

Table 9: Comparison of training time and memory of different models on `Cora` and `Pokec`.

Cora	GCN	GAT	DenseGAT	DIFFORMER-s
Train time (s)	0.0584	0.0807	0.5165	0.1438
Training memory (MB)	1168	1380	8460	1350
Pokec	**GCN**	**GAT**	**DenseGAT**	**DIFFORMER-s**
Train time (s)	1.0698	14.8737	88.0769	2.2066
Training memory (MB)	1812	2014	13174	2923

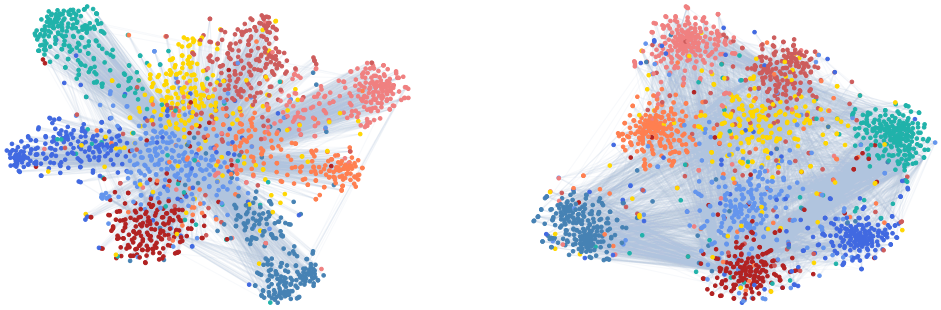

(a) The first layer (b) The last layer

Figure 6: Visualization of instance representations and diffusivity strengths (we set a threshold and only plot the edges with weights more than the threshold) at different layers given by DIFFORMER-s on `20News`.

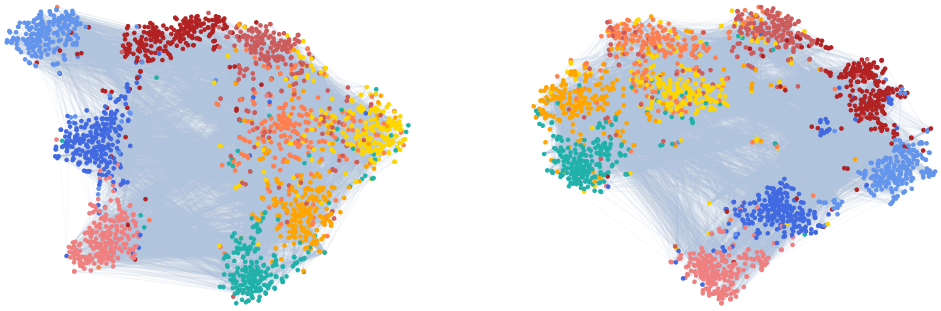

(a) The first layer (b) The last layer

Figure 7: Visualization of instance representations and diffusivity strengths (we set a threshold and only plot the edges with weights more than the threshold) at different layers given by DIFFORMER-s on `STL`.

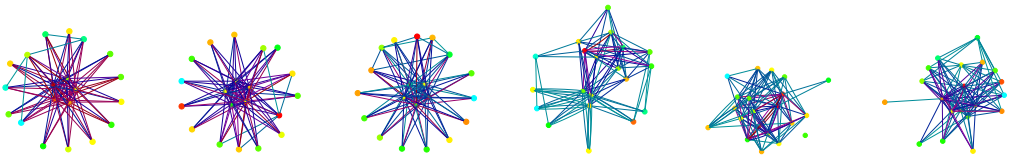

(a) (b) (c) (d) (e) (f)

Figure 8: The produced diffusivity of the first layer (i.e., $\hat{\mathbf{S}}^{(1)}$) on `Chickenpox` across the first three snapshots, yielded by DIFFORMER-s, shown in (a)$\sim$(c), and DIFFORMER-a, shown in (d)$\sim$(f). Node colors correspond to ground-truth labels (i.e., reported cases), varying from red to blue as the label increases. We visualize the edges with top 100 diffusion strength, where edge colors change from blue to red as $\hat{\mathbf{S}}^{(1)}_{ij}$ increases.